Available online at www.sciencedirect.com
ScienceDirect
Comput. Methods Appl. Mech. Engrg. 289 (2015) 498–516
Computer methods in applied mechanics and engineering
www.elsevier.com/locate/cma

Coupled thermo–mechanical interface model for concrete failure analysis under high temperature

Antonio Caggiano*, Guillermo Etse

LMNI, FIUBA, Laboratory of Materials and Structures, Faculty of Engineering, University of Buenos Aires, Argentina
National Scientific and Technical Research Council (CONICET), Argentina

Received 1 July 2014; received in revised form 6 January 2015; accepted 15 February 2015
Available online 23 February 2015

Abstract

A thermo–mechanical interface model for failure analysis of concrete subjected to high temperature is presented in this work. The model is an extension of a fracture energy-based interface formulation which now includes thermal damage induced by high temperature and/or fire. The coupled thermal–mechanical effect in the interface model is taken into account through the formulation of a temperature dependent maximum strength criterion and fracture energy-based softening or post-cracking rule. In this sense, the strong variation of concrete ductility during failure processes in mode I, II or mixed types of fracture is described through the consideration of temperature dependent ductility measures and of the specific work spent in softening. Moreover, a temperature-based scaling function is introduced to more accurately predict the thermal effect affecting the interface strength and post-cracking response. After outlining the mathematical formulation of the interface model, numerical analyses are presented to validate its soundness and capability. A wide range of experimental results, available in the scientific literature, are analyzed at both material and structural scale of analysis using the proposed interface model and in the framework of the discrete crack approach. The results demonstrate the predictive capabilities of the proposed interface constitutive theory for temperature dependent failure behavior of concrete.

Keywords: High temperature; Fracture; Interface; Cracking; Discontinuous approach; Coupled thermo–mechanics

1. Introduction

The exposure to high temperature and fire is one of the most destructive actions that concrete material may suffer [1]. Under elevated temperature, the chemical composition, the physical structure as well as the moisture content of concrete drastically change [2,3]. Such changes deal with the dehydration of hardened cement paste and the conversion of calcium hydroxide into calcium oxide with the subsequent release of bond water to become free water [4,5]. As a consequence, during and after long term exposure to high temperature, the most important mechanical features of concrete can be adversely affected. Experimental evidences demonstrate the substantial changes of cohesion, tensile

* Corresponding author at: National Scientific and Technical Research Council (CONICET), Argentina. Tel.: +54 9 11 62414876.
E-mail addresses: acaggiano@fi.uba.ar (A. Caggiano), getse@herrera.unt.edu.ar (G. Etse).

http://dx.doi.org/10.1016/j.cma.2015.02.016
0045-7825/

and compressive strengths [6,7], Young modulus and Poisson's ratio [8,3] of concrete materials due to the long term exposure to fire and/or high temperature.

The relevance of high temperature exposure and its severe consequences for the safety conditions and integrity of concrete structures is well recognized by several design codes which, at the same time, provide simplified guidelines or rules for the concrete design under elevated temperature, see a.o. the ACI-216.1-07 [9] and EN-1992-1.2 [10].

Several theoretical models are currently available in the scientific literature to simulate the failure processes of concrete structures subjected to the combined action of high temperatures and mechanical loads. Most of the existing proposals follow the so-called smeared crack approach. As a reference we may report the works by Nechnech et al. [11] who describe an elastic–plastic damage model for plain concrete subjected to high temperature, by Schrefler et al. [12] and Pont et al. [13] who take into account the thermo-hydro-mechanical effect in the description of concrete behavior at elevated temperature and also by Tenchev and Purnell [14] whereby an application of a damage constitutive theory is performed for predicting spalling phenomena in concrete.

In this work, and in the framework of the discrete crack approach, an elasto–thermo–plastic interface model is proposed to predict the concrete cracking and failure behavior when subjected to combined thermo–mechanical actions under high temperature.

Zero-thickness interface elements, formulated in terms of contact stresses versus opening relative displacements, have been historically employed for modeling both the response behavior of material discontinuities such as mechanical contacts [15,16], bonds [17–19] and crack evolutions in quasi-brittle materials like concrete [20,21]. Also, several plasticity-based interface formulations have been proposed to predict failure behaviors of discontinuities in soil/rock mechanisms [22]. One of the most frequent use of interface elements in computational concrete mechanics is related to mesoscopic failure simulations. Thereby, the use of non-linear interfaces can be limited to model the aggregate-mortar joints [23]. This strategy is combined with the use of non-linear continuum models for the mortar in between aggregates. Alternatively, the use of non-linear interfaces may involve both the aggregate–mortar and the mortar–mortar joints while linear elastic models are considered for the continuum mortar elements. This strategy was proposed by Lopez et al. [24,25] for rate independent failure behavior analysis of concrete and by Lorefice et al. [26] for time dependent simulations of concrete failure behavior. Recently, the approach and interface model by Lopez et al. [24,25] was extended by the authors, see [27–29], to model the behavior of mortar-to-mortar interfaces of fiber reinforced cementitious composites. Regarding the modeling of transport problems in concrete through interfaces we may refer here to the works by Segura and Carol [30] who take into account moisture diffusion problems and coupled analysis, the fluid flow through discontinuities by Idiart et al. [31] which is related to coupled hygro-mechanical analysis of concrete drying shrinkage, the proposal by Idiart et al. [32] whereby a chemo-mechanical analysis of concrete cracking and degradation due to external sulfate attack is performed, and by Liaudat et al. [33] who outline a diffusion–reaction model for Alkali–Silica Reaction (ASR) processes.

The elasto–thermo–plastic interface model proposed in this work is used in computational analysis of concrete materials and related structures when subjected to long term exposure of high temperatures. The interface model is formulated within the general framework of the flow theory of plasticity which is embedded in fracture mechanics concepts to account for the objectivity of the fracture energy release during post-peak regimes of concrete. Based on the original model by Carol et al. [34], the interface formulation is extended to take into account the temperature effects in the maximum strength criterion and in the softening rules under both mode I and mode II types of failure, which are differently and independently treated in the constitutive model. A relevant novel aspect in this interface model formulation is the inclusion of the thermal effects in the softening rules. It is worth mentioning that under monotonic thermo–mechanical loading, the increasing damage of cohesive-frictional materials like concrete gives rise to the development of macroscopic cracks representing first order discontinuities of both displacement and thermal fields. Therefore, the fixed (discrete) crack approach, based on coupled thermo–mechanical interfaces, represents the most straightforward and direct procedure to model jumps of velocities and thermal rate fields in quasi-brittle materials like concrete. A fundamental advantage of this approach, based on zero-thickness interfaces, is the related objectivity of the Finite Element (FE) predictions of localized failure processes regarding mesh-size and orientation, provided when a sufficient and appropriated mesh density is considered. An additional advantage of zero thickness interfaces is the inexistence of element locking which constitutes a relevant shortcoming of "thin-layer" FEs.

It is important to remark that strength criterion degradation due to temperature effects is strictly related to the interaction between drying shrinkage, high temperature and cement (de-)hydration. Actually, a classical way for modeling drying processes in porous media like concrete deals with calculating the moisture diffusion which takes place in

its porous structure. Particularly, this can be approached through modeling the migration of the "evaporable water" present in the pore structure of the cementitious composite: it can be derived as the difference between the "total amount of water" (present into the pores) and the "non-evaporable one" [35]. The last is mainly dependent on the degree of the cements hydration or (de-)hydration [36,37], for the cases of young concrete or concrete subjected to high temperature, respectively. Thus, the interaction between drying shrinkage [31], high temperature and cement (de-)hydration [38] represents a very interesting topic to be investigated. However, to take into account such a complex phenomena, in the framework of the interface theory presented in this work, it is necessary to further extend the formulation into the domain of combined diffusion-driven and cement hydration phenomena, hence, considering moisture diffusion through both the porous continuum and the interfaces. This further development will be certainly considered by the authors in the next extension of the thermo–mechanical interface theory for concrete proposed in this work.

After a brief literature review, Section 2 summarizes the mathematical formulation of the elasto–thermo–plastic interface model proposed in this work. The post-cracking softening rule based on both thermal effects and fracture work spent is highlighted in Section 3. The classical elasto–thermo–plastic rate equations are then described in Section 4, while the heat transfer phenomenon throughout an opened interface is reported in Section 5. Finally, Section 6 deals with the validation of the proposed model and evaluates its numerical predictions on a series of experimental results which are often assumed as reference for computational simulations at material and structural analysis scale. After presenting the concluding remarks, in the Appendix there is summarized the flowchart of local Newton's method employed for the elasto–thermo–plastic interface model proposed in this work.

2. Coupled fracture-based thermal model for plain mortar/concrete interface

This section reports the temperature dependent interface formulation aimed at analyzing cracking behavior of quasi-brittle materials like cementitious mortar and concrete. The basic constitutive equations of the proposed elasto–thermo–plastic interface model are

$$\begin{aligned} \dot{\mathbf{u}} &= \dot{\mathbf{u}}^{el} + \dot{\mathbf{u}}^{cr} + \dot{\mathbf{u}}^{th} \\ \dot{\mathbf{u}}^{el} &= \mathbf{C_d}^{-1} \cdot \dot{\mathbf{t}} \\ \dot{\mathbf{t}} &= \mathbf{C_d} \cdot \left(\dot{\mathbf{u}} - \dot{\mathbf{u}}^{cr} - \dot{\mathbf{u}}^{th} \right) \end{aligned} \tag{1}$$

where $\dot{\mathbf{u}} = [\dot{u}, \dot{v}]^t$ is the vector of relative displacement rates across the interface which is additively decomposed into the elastic, plastic and thermal components, $\dot{\mathbf{u}}^{el}$, $\dot{\mathbf{u}}^{cr}$ and $\dot{\mathbf{u}}^{th}$, respectively; $\dot{\boldsymbol{t}} = [\dot{\sigma}_N, \dot{\sigma}_T]^t$ is the stress rate vector defined in interface coordinates, σ_N and σ_T, being the normal and shear components, respectively. Moreover, $\mathbf{C_d}$ defines the elastic stiffness matrix, thermally degraded through the temperature-based scalar variable, d_τ,

$$\mathbf{C_d} = d_\tau \mathbf{C} \quad \text{with} \quad \mathbf{C} = \begin{pmatrix} k_N & 0 \\ 0 & k_T \end{pmatrix} \tag{2}$$

where k_N and k_T are the interface normal and tangential elastic stiffness, respectively.

2.1. Thermal interface displacements

Besides the classical interface assumptions, dealing with the jumps of normal and tangential displacements (kinematic discontinuities) and the continuity of the interface stresses, it is assumed in this proposal that the temperature field also exhibits a discontinuity across the interface due to a strong jump of the interface normal kinematic. This follows the original proposal by Willam et al. [39]. Particularly, the rate of the relative joint displacements due to thermal effects, $\dot{\mathbf{u}}^{th}$, is assumed to be linearly related to the rate of the temperature jump across the interface, $\Delta\dot{T}$,

$$\begin{aligned} \dot{u}^{th} &= \alpha_s^0 \left[\left| \Delta \dot{T} \right| \right] \\ \dot{v}^{th} &= \alpha_s^0 \left[\left| \Delta \dot{T} \right| \right] \end{aligned} \tag{3}$$

where α_s^0 is a coefficient of superficial thermal expansion while the norm of the temperature jump (across the interface) is indicated as $[|\Delta T|] = \left[\left| T^+ - T^- \right| \right]$, T^+ and T^- being the temperature at the $+$ and $-$ side of the considered interface.

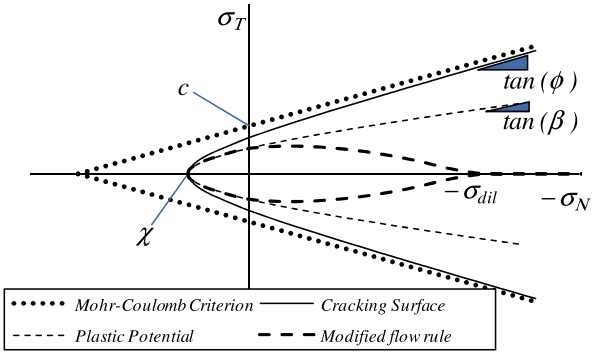

Fig. 1. Failure hyperbola by Carol et al. [34], Mohr–Coulomb surface, plastic potential and modified flow rule.

Above expression in vectorial form can be expressed as

$$\dot{\mathbf{u}}^{th} = \alpha_s^0 \left[\left| \Delta \dot{T} \right| \right] \mathbf{i} \tag{4}$$

with $\mathbf{i} = [1, 1]$.

2.2. Rate of interface relative plastic displacement

The vector of relative plastic displacement rates, according to a non-associated flow rule, can be defined as

$$\dot{\mathbf{u}}^{cr} = \dot{\lambda} \mathbf{m} \tag{5}$$

where $\dot{\lambda}$ is the non-negative plastic multiplier which derives from the classical Kuhn–Tucker loading/unloading and consistency conditions

$$\begin{array}{lll} \dot{\lambda} \geq 0, \quad f \leq 0, \quad \dot{\lambda} f = 0 & \text{Kuhn–Tucker} \\ \dot{f} = 0 & \text{Consistency} \end{array} \tag{6}$$

$f = f[\sigma_N, \sigma_T]$ being the yield condition of the model while $\mathbf{m}$ the vector controlling the direction of interface fracture displacements.

2.3. Temperature dependent yielding criterion

Yielding surface is defined by means of the following three-parameter criterion (outlining the hyperbola represented in Fig. 1)

$$f = \sigma_T^2 - (c - \sigma_N \tan\phi)^2 + (c - \chi \tan\phi)^2 \tag{7}$$

where the tensile strength χ (vertex of the hyperbola), the cohesion c and the frictional angle ϕ are internal parameters defining the evolution of the interface strength surface under thermal and mechanical loading.

Eq. (7) outlines two main failure modes:

- *Mode I type of fracture*: maximum strength capacity of the interface is reached under direct tensile stress, corresponding to the intersection between the strength surface and the normal stress axis.
- *Mode II type of fracture*: maximum strength capacity is approached under combined shear and normal stresses. These stress states are located along the asymptotic zone of the maximum strength surface of the interface, where the hyperbola approximates the well-known Mohr–Coulomb criterion (see Fig. 1).

2.4. Plastic flow rule

The direction of the non-associated plastic flow $\mathbf{m}$, defining the rate of the interface fracture displacements in Eq. (5), is obtained from

$$\mathbf{m} = \mathbf{A} \cdot \mathbf{n} \tag{8}$$

where

$$\mathbf{n} = \frac{\partial f}{\partial \mathbf{t}} = \left[\frac{\partial f}{\partial \sigma_{\mathbf{N}}}, \frac{\partial f}{\partial \sigma_{\mathbf{T}}}\right]^{\mathbf{t}} = [\mathbf{2}\tan\phi(\mathbf{c} - \sigma_{\mathbf{N}}\tan\phi), \mathbf{2}\sigma_{\mathbf{T}}]^{\mathbf{t}} \tag{9}$$

being the direction of the associated plastic flow. Then, the transformation matrix $\mathbf{A}$ in Eq. (8) is

$$\mathbf{A} = \begin{cases} \begin{pmatrix} \dfrac{\tan\beta}{\tan\phi} & 0 \\ 0 & 1 \end{pmatrix} & \text{if } \sigma_N \geq 0 \\ \begin{pmatrix} \left[1 - \dfrac{|\sigma_N|}{\sigma_{dil}}\right]\dfrac{\tan\beta}{\tan\phi} & 0 \\ 0 & 1 \end{pmatrix} & \text{if } -\sigma_{dil} \leq \sigma_N < 0 \\ \begin{pmatrix} 0 & 0 \\ 0 & 1 \end{pmatrix} & \text{if } \sigma_N < -\sigma_{dil} \end{cases} \tag{10}$$

where $\tan\beta$ is the dilation angle of the plastic potential as highlighted in Fig. 1 with $0 \leq \tan\beta \leq \tan\phi$. Thereby, the parameter σ_{dil} represents the normal stress at which the dilatancy vanishes, see Caggiano et al. [27].

3. Temperature and fracture-energy dependent evolution law

In this proposal a unified decay function is considered to soften all internal parameters controlling the interface yield criterion of Eq. (7) as follows

$$p_i = g_1\left(S[\xi_{p_i}]\right) g_2\left(\mathrm{H}[\psi_{p_i}]\right) p_{0i} \tag{11}$$

where p_i alternatively represents χ, c and $\tan\phi$.

Eq. (11) defines the typical degradation law of the internal parameters from their maximum (or initial) values, $p_i = p_{0i}$, to the residual ones. In this sense, the following scaling functions are proposed for taking into account fracture processes caused by mechanical or thermal effects

$$g_1\left(S[\xi_{p_i}]\right) = \left(1 - \left(1 - r_{pi}\right) S[\xi_{p_i}]\right) \quad \text{mechanical,} \tag{12}$$

and

$$g_2\left(\mathrm{H}[\psi_{p_i}]\right) = \left(1 - \left(1 - t_{pi}\right) \mathrm{H}[\psi_{p_i}]\right) \quad \text{thermal,} \tag{13}$$

where r_{pi} and t_{pi} measure the residual amounts of the internal parameters under mechanical or thermal loadings, respectively.

3.1. Fracture scaling function

The scaling function $S[\xi_{p_i}]$ in Eqs. (11) and (12) is defined by means of the following relationship

$$S[\xi_{p_i}] = \frac{e^{-\alpha_{p_i}}\xi_{p_i}}{1 + (e^{-\alpha_{p_i}} - 1)\xi_{p_i}} \tag{14}$$

whereby parameter α_{p_i} controls the decay form of the internal parameter, as shown in Fig. 2, while the non-dimensional variable ξ_{p_i} introduces the influence of the ratio between the plastic work currently spent and the available fracture energy in mode I or II (G_f^I or G_f^{IIa}) according to the following C^1 continuity function proposed by Caballero et al. [40]

$$\xi_\chi = \begin{cases} \dfrac{1}{2}\left[1 - \cos\left(\dfrac{\pi w_{cr}}{G_f^I}\right)\right] & \text{if } w_{cr} \leq G_f^I \\ 1 & \text{otherwise,} \end{cases} \tag{15}$$

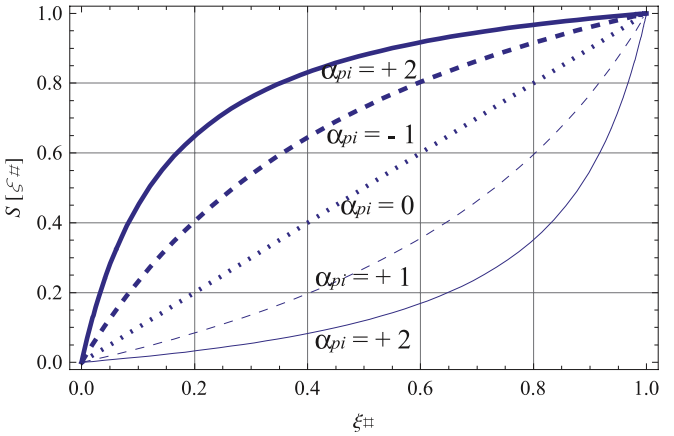

Fig. 2. Scaling function $S[\xi_{p_i}]$ considering different values of α_{p_i}.

$$\xi_c = \xi_{\tan\phi} = \begin{cases} \dfrac{1}{2}\left[1 - \cos\left(\dfrac{\pi\, w_{cr}}{G_f^{IIa}}\right)\right] & \text{if } w_{cr} \le G_f^{IIa} \\ 1 & \text{otherwise.} \end{cases} \tag{16}$$

The fracture work spent, w_{cr}, during an opening-sliding fracture process, controls the evolutions of the material parameters χ, c and $\tan\phi$ in softening regime of the interface response. The variable w_{cr} defines the necessary amount of released energy to open a single crack in tensile and/or shear fracture mode due to normal σ_N and/or tangential σ_T joint stresses.

Therefore, the rate of the fracture work spent $\dot{w}_{cr}$, during a generic fracture process, is defined as follows

$$\begin{aligned} \dot{w}_{cr} &= \sigma_N \cdot \dot{u}^{cr} + \sigma_T \cdot \dot{v}^{cr}, \quad \text{if } \sigma_N \ge 0 \\ \dot{w}_{cr} &= [\sigma_T - |\sigma_N| \tan(\phi)] \cdot \dot{v}^{cr}, \quad \text{if } \sigma_N < 0 \end{aligned} \tag{17}$$

then, the total dissipated work is obtained by integrating the fracture work increments during the entire fracture process.

3.2. Temperature-based scaling rule

The $g_2\left(\mathrm{H}[\psi_{p_i}]\right)$ function in Eq. (11) is the proposed temperature-based rule. It is based on the temperature-based law $\mathrm{H}[\psi_{p_i}]$ outlined in Eq. (13) and expressed as

$$\mathrm{H}[\psi_{p_i}] = \frac{e^{-\varsigma_{p_i}}\,\psi_{p_i}}{1 + (e^{-\varsigma_{p_i}} - 1)\psi_{p_i}} \tag{18}$$

where ς_{p_i} defines several possible decay forms of the temperature-based softening description (Fig. 3), while ψ_{p_i} is a thermal depending parameter defined as follows

$$\psi_{p_i} = \frac{1 - \cos\left(\pi \frac{T_{avg} - T_{avg,0}}{T_{avg,f} - T_{avg,0}}\right)}{2} \tag{19}$$

where

$$T_{avg} = \frac{T^+ + T^-}{2} \tag{20}$$

being the average temperature in the interface plane, while $T_{avg,0}$ and $T_{avg,f}$ are two input temperatures to be calibrated. Particularly, when $T_{avg} < T_{avg,0}$ (low temperature tests) the case of temperature insensitive interface is obtained, while when $T_{avg} > T_{avg,f}$ (elevated temperatures) the case of totally softened interface due to thermal effects is considered.

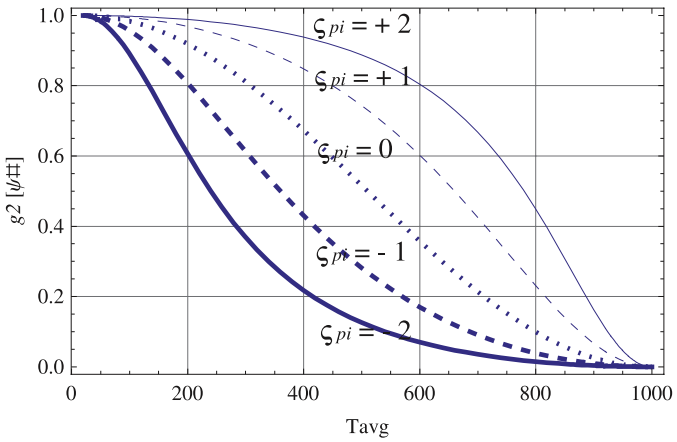

Fig. 3. Temperature-based interface rule $g_2\left(\mathrm{H}[\psi_{p_i}]\right)$ vs. T_{avg}: as example $T_{avg,0} = 20\,^{\circ}\mathrm{C}$, $T_{avg,f} = 1000\,^{\circ}\mathrm{C}$ and all $t_{pi} = 0$.

In this article, the same temperature-based law of Eq. (13) has been also employed to describe the thermal damage, d_τ, controlling the interface stiffness decay in Eq. (2) due to thermal effects.

4. Elasto-thermo-plastic rate equations

The interface elasto–thermo–plastic rate equations are obtained starting from the consistency condition of Eq. (6)

$$\frac{\partial f}{\partial \mathbf{t}}\dot{\mathbf{t}} + \frac{\partial f}{\partial \dot{\lambda}}\dot{\lambda} + \frac{\partial f}{\partial T_{avg}}\dot{T}_{avg} = 0 \tag{21}$$

where the softening parameters due to mechanical and thermal effects can be derived as

$$\bar{H} = -\frac{\partial f}{\partial \dot{\lambda}} = -\frac{\partial f}{\partial p_i}\frac{\partial p_i}{\partial w_{cr}}\frac{\partial w_{cr}}{\partial \mathbf{u}^{cr}}\mathbf{m} \tag{22}$$

and

$$I = -\frac{\partial f}{\partial T_{avg}} = -\frac{\partial f}{\partial p_i}\frac{\partial p_i}{\partial T_{avg}} \tag{23}$$

respectively.

The rate of the plastic multiplier follows from the combination between Eqs. (21), (1), (22) and (23)

$$\dot{\lambda} = \frac{\frac{\partial f}{\partial \mathbf{t}} \cdot \mathbf{C_d} \cdot \dot{\mathbf{u}} - \alpha_s^0 \left[\left|\Delta \dot{T}\right|\right] \frac{\partial f}{\partial \mathbf{t}} \cdot \mathbf{C_d} \cdot \mathbf{i} - I\,\dot{T}_{avg}}{\bar{H} + \frac{\partial f}{\partial \mathbf{t}} \cdot \mathbf{C_d} \cdot \mathbf{m}}. \tag{24}$$

Consequently, the rate of normal and tangential interface stresses is derived through the rates of relative displacement vector and temperature rise as

$$\dot{\mathbf{t}} = \mathbf{C_d}^{ep} \cdot \dot{\mathbf{u}} - \mathbf{f}[\dot{T}]. \tag{25}$$

Particularly, the tangential interface stiffness for elastic degradation expands into

$$\mathbf{C_d}^{ep} = \left[\mathbf{C_d} - \frac{\mathbf{C_d} \cdot \mathbf{m} \otimes \mathbf{n} \cdot \mathbf{C_d}}{\bar{H} + \mathbf{n} \cdot \mathbf{C_d} \cdot \mathbf{m}}\right] \tag{26}$$

while the thermal interface stresses due to the rate of interface temperature field are

$$\mathbf{f}[\dot{T}^+, \dot{T}^-] = \alpha_s^0 \left[\left|\Delta \dot{T}\right|\right] \mathbf{C_d} \cdot \mathbf{i} - \frac{\alpha_s^0 \left[\left|\Delta \dot{T}\right|\right] \mathbf{C_d} \cdot \mathbf{m} \otimes \mathbf{n} \cdot \mathbf{C_d}\mathbf{i} + I\dot{T}_{avg}\mathbf{C_d} \cdot \mathbf{m}}{\bar{H} + \mathbf{n} \cdot \mathbf{C_d} \cdot \mathbf{m}}. \tag{27}$$

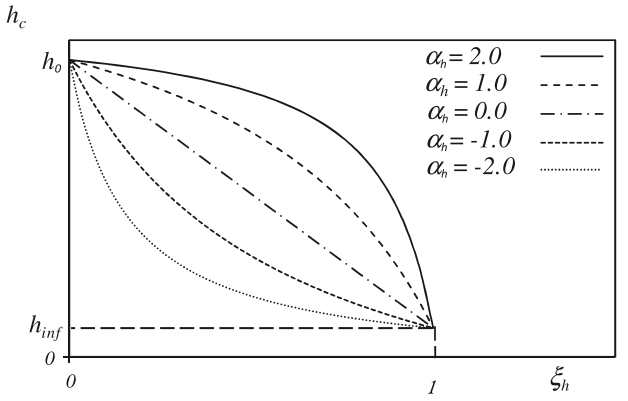

Fig. 4. Degradation description of the convective heat transfer coefficient h_c in function of the normal crack opening displacement across the interface.

The Appendix of the paper highlights the flowchart of local Newton's method employed for the elasto–thermo–plastic interface model proposed in this work.

5. Heat transfer across interface

Heat transfer throughout an opened interface is governed by means of the following convective interface rule [39]

$$q_n = -h_c\,[|\Delta T|] \tag{28}$$

assuming a discontinuity of the temperature field

$$[|\Delta T|] = \left[\left|T^+ - T^-\right|\right] \neq 0 \tag{29}$$

while h_c is the convective heat transfer coefficient. Its value mainly depends on the normal positive separation (u^+) of the interface

$$h_c = h_c\left(u^+\right), \quad h_0 \geq h_c \geq h_{\text{inf}} \tag{30}$$

where h_c varies between a maximum value h_0, related to the thermal conductivity for a "closed crack", and a minimum one h_{inf} which denotes the convective heat transfer coefficient for an "open crack" (Fig. 4).

Hereby, the following expression for h_c has been considered

$$h_c = \begin{cases} h_0 & \text{if } u < 0 \\ (h_0 - h_{\text{inf}})\left(1 - \dfrac{e^{-\alpha_h \xi_h}}{1 - \left(1 - e^{-\alpha_h}\right)\xi_h}\right) + h_{\text{inf}} & \text{if } 0 \leq u \leq \bar{u} \\ h_{\text{inf}} & \text{if } u > \bar{u} \end{cases} \tag{31}$$

α_h being a parameter which describes the decay form of h_c, as shown in Fig. 4, whereas the non-dimensional variable

$$\xi_h = \frac{u^+}{\bar{u}} \tag{32}$$

introduces the influence of the ratio between current interface opening and its maximum possible value which is described through the comparison parameter $\bar{u}$ (to be experimentally calibrated).

6. Numerical analyses

This section proposes some numerical applications considering concrete specimens submitted to high temperature. Firstly, and for calibration purposes, experimental results on concrete prisms tested under pure uniaxial tension are considered. Then, numerical analyses are performed to verify the predictive capabilities of the proposed interface model. Particularly, failure behavior of three-point bending and direct shear tests on concrete components at residual stage (after they were subjected to high temperature fields) is considered.

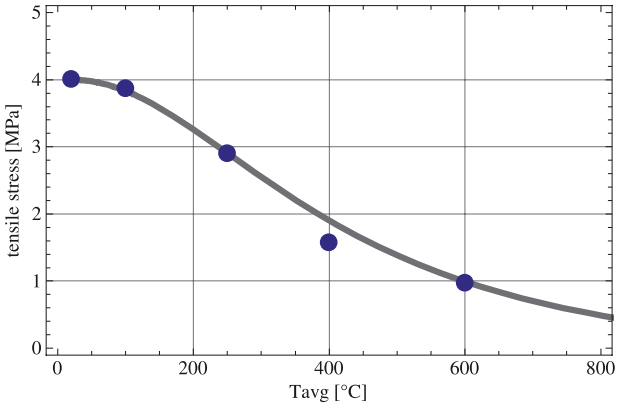

Fig. 5. Strength decay in direct tensile tests: comparison between experimental results [41] and model predictions.

6.1. Interface model calibration

The tensile tests performed on concrete specimens after they were subjected to room, medium and high temperatures (residual stages) presented by Bamonte and Felicetti [41] are considered as reference. As a result of the calibration analysis, the following model parameters were adopted: $k_N = 500\,\text{MPa/mm}$, $k_T = 200\,\text{MPa/mm}$, $\tan\phi_0 = 0.6$, $\tan\beta = 0.3$, $r_{\tan\phi} = 0.67$, $\chi_0 = 4.0\,\text{MPa}$, $c_0 = 7.0\,\text{MPa}$, $G_f^I = 0.15\,\text{N/mm}$, $G_f^{IIa} = 1.5\,\text{N/mm}$, $\sigma_{dil} = 10\,\text{MPa}$, $\alpha_\chi = 0.5$, $T_{avg,0} = 20\,^\circ\text{C}$, $T_{avg,f} = 1500\,^\circ\text{C}$, $\varsigma_\chi = \varsigma_{d_\tau} = -1.8$. All other interface parameters were considered null.

The calibrated decay trends of both tensile strength and elastic stiffness which are shown in Figs. 5 and 6 exhibit similar behavior against increasing temperatures.

Fig. 5 compares the variation of concrete peak strength with temperature, obtained from the direct tensile tests by Bamonte and Felicetti [41] with the numerical prediction based on the interface model parameters and its internal decay functions as indicated above.

Then, the comparison between the same experimental results and numerical data in terms of stresses vs. crack opening displacements, for three different temperature levels, is highlighted in Fig. 7. Beyond the general soundness of the interface model predictions for failure behavior of concrete affected by temperature, the numerical results demonstrate the capabilities of the proposed formulation to reproduce the strong sensitivity of concrete mechanical behavior on the acting temperature. When submitted to high temperatures, concrete presents a relevant tensile strength decay with progressive transitions from brittle to increasing ductile post-peak responses.

6.2. Predictive analysis of failure behavior under mixed-mode of fracture

To analyze the model predictions of concrete failure behavior subjected to temperature and general mixed-modes of fracture, the stress histories on plane concrete panels by Hassanzadeh [42] are considered.

These experimental tests have been performed on prismatic concrete specimens of $70 \times 70\,\text{mm}^2$ cross section with a 15 mm deep notch along their perimeters (Fig. 8). In those tests, both normal and transversal relative displacements are co-imposed to the two parts (bottom and top parts of Fig. 8) of the notched specimen with the aim of reproducing cracking processes in concrete under mode I and II types of fracture depending on the angle between the two prescribed displacement components. During the first part of these tests only normal tensile displacements u are applied until the peak strength is reached. In the second part of the test, tensile displacements are combined with transversal ones v applied on the upper part of the notched specimen and defining a pre-fixed angle ($\tan\theta = u/v$). The experimental tests by Hassanzadeh [42] were performed under room temperature. In this numerical analysis the effect of temperature on the overall failure behavior of the notched concrete panels is evaluated.

Two different cases are evaluated: i.e., $\theta = 60^\circ$ and $\theta = 30^\circ$. For each load angle three levels of temperature are considered: room temperature $T = 20\,^\circ\text{C}$, intermediate temperature $T = 250\,^\circ\text{C}$ and high temperature $T = 600\,^\circ\text{C}$.

Figs. 9–10 and 11–12 show the model predictions in terms of both normal stress vs. u curves and of shear stress vs. v curves, corresponding to the cases $\theta = 30^\circ$ and 60°, respectively. The numerical results take into account the three different temperatures. The same parameters obtained in the model calibration, see Section 6.1, are used. These results

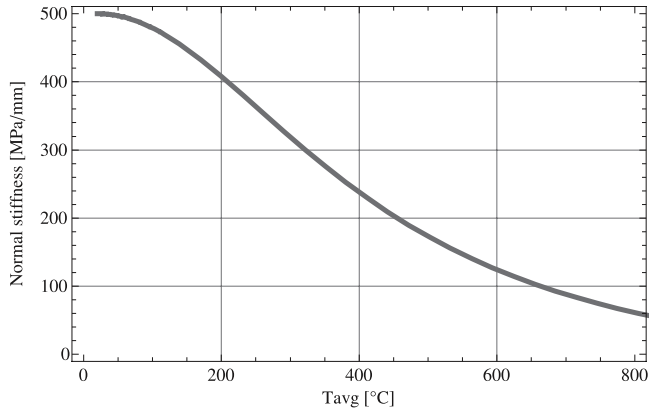

Fig. 6. Elastic modulus decay and its relation with the temperature.

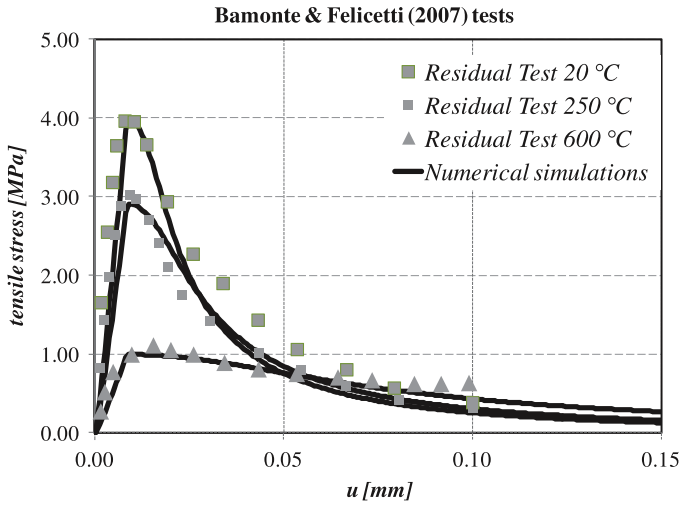

Fig. 7. Residual stress–crack opening curves: experimental results against numerical predictions.

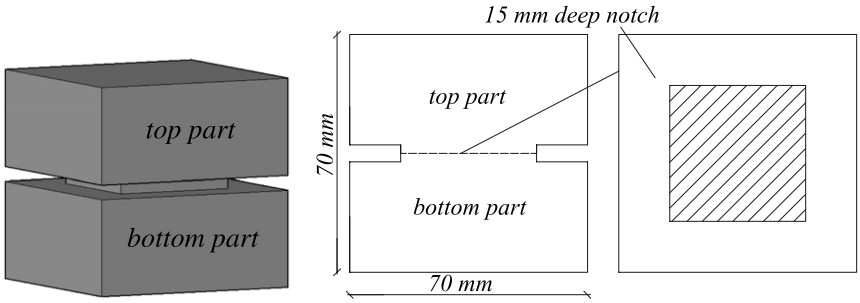

(a) 3D view. (b) Geometric details.

Fig. 8. Concrete specimen of Hassanzadeh tests [42].

demonstrate an acceptable capability of the interface model to reproduce failure processes under room temperature against the experimental results by Hassanzadeh [42]. The results under medium and high temperatures illustrate the significant temperatures influence on the peak strength and post-peak ductility of the concrete panel failure responses. The residual stress is practically not affected by temperature. This is reasonable as the friction of the fine aggregate, which controls the concrete residual strength, is less sensitive to temperature.

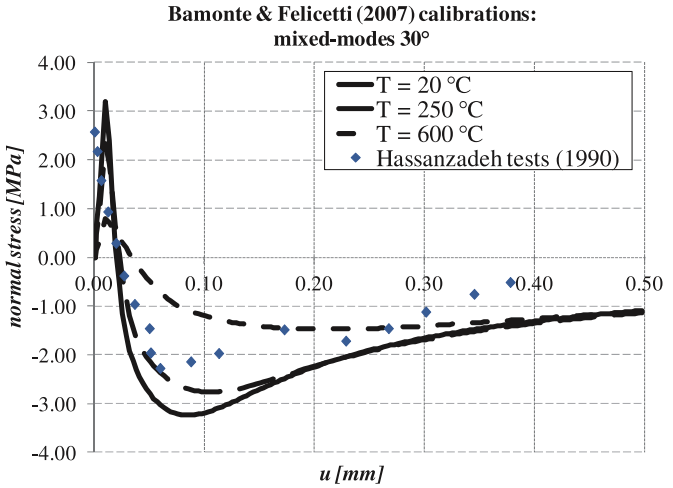

Fig. 9. Hassanzadeh [42] tests for $\theta = 30°$: normal stress vs. relative normal displacement. Experimental results under room temperature and numerical results under different temperatures.

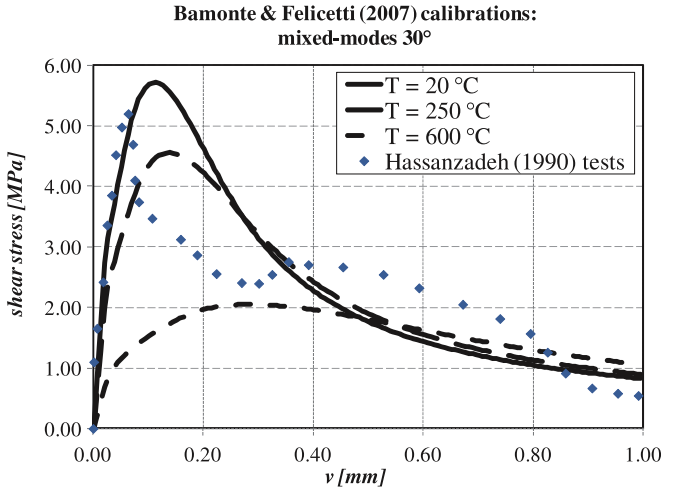

Fig. 10. Hassanzadeh [42] tests for $\theta = 30°$: shear stress vs. relative tangential displacement. Experimental results under room temperature and numerical results under different temperatures.

6.3. *FE analysis of three-point bending tests*

In this section, the predictions of the temperature-based interface model are evaluated against pre-notched concrete beams subjected to thermal effects and tested under three-point bending. The discontinuous model was calibrated with the experimental data of residual mechanical properties obtained in the tests performed by Barragan et al. [43].

Such specimens were exposed to different maximum thermal and cooling regimes. Particularly, concrete beams were subjected to different maximum temperatures from ambient (20 °C about) to high temperature (700 °C). An electric furnace with automatic temperature control was used for this purpose. The heating rate, measured with thermocouples inserted in the concrete specimens, was 100 °C/h about. The maximum temperature was kept constant during an hour for each beam. Then, two kinds of cooling regimens were alternatively applied: the first one leaving the specimens in the furnace for a slow cooling while for the other type the beams were rapidly cooled with spurts of cold water during half an hour. A concrete mixture, tested at ambient temperature, was also analyzed by Barragan et al. [43] as reference. For the numerical validation, only experimental results of concrete beams cooled with water system were considered.

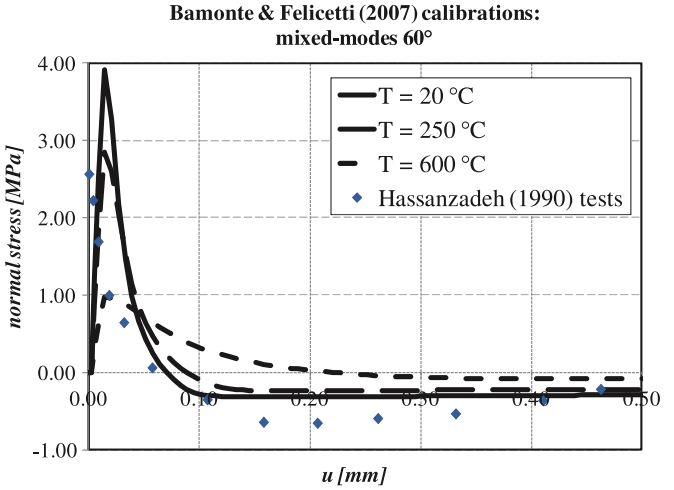

Fig. 11. Hassanzadeh [42] tests for $\theta = 60°$: normal stress vs. relative normal displacement. Experimental results under room temperature and numerical results under different temperatures.

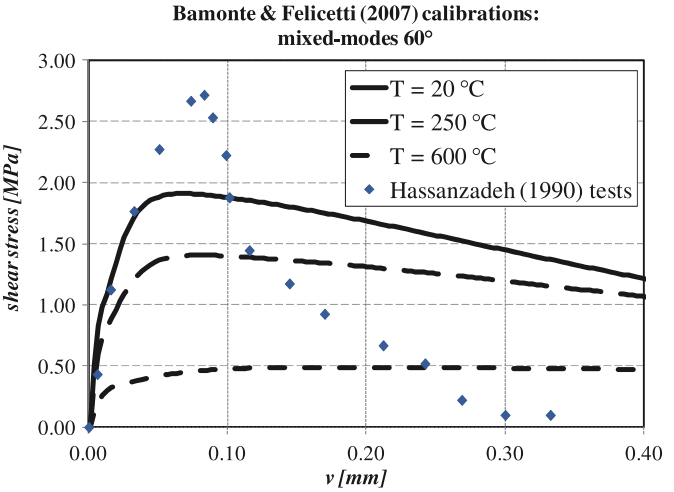

Fig. 12. Hassanzadeh [42] tests for $\theta = 60°$: shear stress vs. relative tangential displacement. Experimental results under room temperature and numerical results under different temperatures.

The simulation of $75 \times 100 \times 400$ mm^3 notched concrete specimens tested under three-point bending according to Barragan et al. [43] described above is performed in this subsection. Plane stress hypothesis and displacement-based control are assumed. The specimens present a vertical notch (2.0 mm wide and a depth of about 50 mm) at the bottom of the beam and at mid-length of the distance between the beam-end supports.

Fig. 13 shows the 2-D geometry of the considered structure while Fig. 14 highlights the FE discretization employed in present analysis. Coupled displacement-temperature 3-node triangles have been adopted in the FE mesh and modeled through a thermo-elastic model, whereas all non-linearities are concentrated within zero-thickness interface elements defined throughout the adjacent edges of the finite elements in the notch zone. Non-linear coupled fracture-based thermal laws were introduced in those interface elements according to the formulation outlined in this work.

Thus, for the purpose of the numerical evaluations, two material models were considered: (i) thermo-elastic material for concrete (mainly describing the continuous elements) and (ii) coupled elasto–thermo–plastic interface model (for interface elements). The key geometric and material properties were chosen according to the experimental evidences by Barragan et al. [43]. Based on the calibration procedure, the elastic modulus and Poisson's ratio of

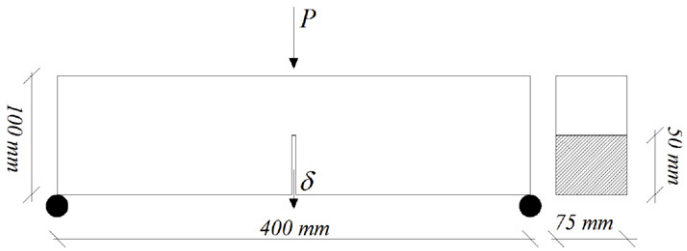

Fig. 13. Specimen geometry according to Barragan et al. [43] test.

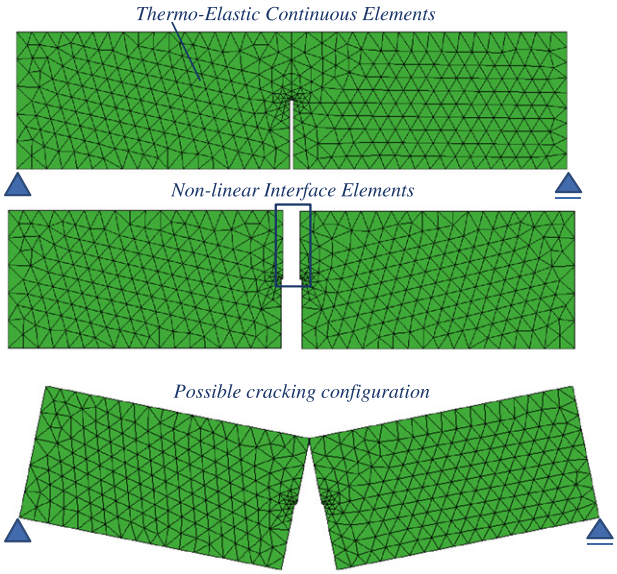

Fig. 14. Finite element mesh, interfaces and possible cracked configuration of the three-point bending.

Table 1
Interface parameters employed in the structural scale analyses: the three-point bending and direct shear tests.

	k_N (MPa/mm)	k_T (MPa/mm)	$\tan\phi_0$	$\tan\beta$	$r_{\tan\phi}$	χ_0 (MPa)	c_0 (MPa)	G_f^I (N/mm)	G_f^{IIa} (N/mm)	σ_{dil} (MPa)	α_χ	$T_{avg,0}$ (°C)	$T_{avg,f}$ (°C)	ζ_χ	d_τ	t_{Tc}
3-Point bending	500.0	200.0	0.6	0.3	0.67	4.0	7.0	0.3	3.0	10.0	0.5	20	1500	−2.0	1.0	0.00
Direct shear				0.4	0.84											0.14

All remaining parameters of interface model were considered null.

concrete modeled as a thermo-elastic medium were given in terms of tabulated data and plotted in Fig. 15. Then, the mechanical parameters of the interface model are listed in Table 1.

Fig. 16 shows the force–deflection curves against corresponding experimental results. It can be observed that the post-cracking response is well captured through the considered discontinuous approach based on non-linear interfaces. The load–displacement responses of concrete under ambient environment or exposed to high temperatures emphasize the significant influence of the thermal effects on the peak strength and post-peak behavior of such specimens loaded under three-point bending. When concrete is subjected to high temperature, both numerical and experimental results demonstrate that the 3-point bending post-peak response turns much more ductile. However, and due to the global deterioration produced by the temperature-based softening phenomenon, a significant decrease of the flexural strength takes place in the analyzed three-point bending tests.

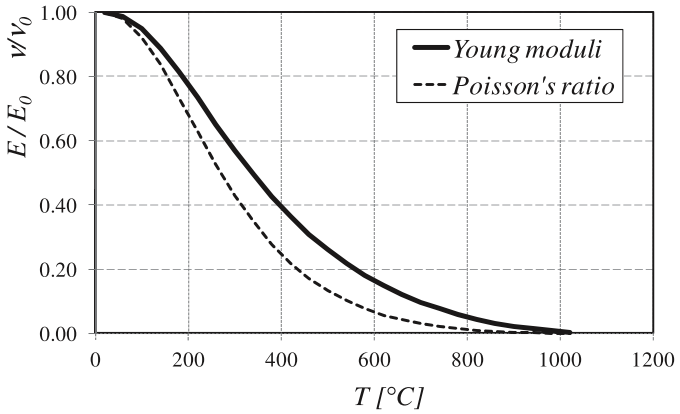

Fig. 15. Variation of the elastic modulus and Poisson's ratio with the temperature: $E_0 = 21698$ MPa and $\nu = 0.17$. (Elastic Modulus and Poisson's ratio of reference at 20 °C.)

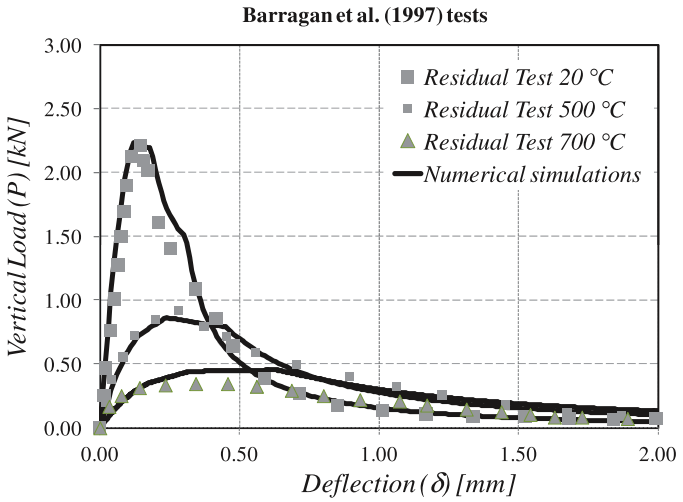

Fig. 16. Load–deflection behavior of three-point beam with central notch: experimental results [43] vs. numerical predictions.

6.4. Direct shear test

In these last analyses the direct shear test shown in Fig. 17 on concrete specimens subjected to elevated temperatures is considered. The same material parameters of the continuum elements employed for the three-point bending problem of previous subsection are considered. Furthermore, a slight variation of the interface parameters was considered in these numerical simulations as reported in Table 1.

Main purpose of these analyses is to evaluate the capability of the proposed interface formulation to predict at the macroscopic level of observation, the sensitivity to temperature of concrete failure behavior in direct shear. Non-linear interfaces are included along contact lines between continuum finite elements in the notch zone as proposed in Fig. 18.

Fig. 19 shows the numerical predictions of the shear load vs. displacement curves corresponding to specimens subjected to different temperatures. The well-known combined phenomena caused by temperature such as strength decrease, increasing post-peak ductility and temperature insensitive residual strength are clearly observed also in this case. The discontinuity in the ascending branch of the load–displacement curves corresponding to the numerical results in Fig. 19 is due to both the sequential (and not simultaneous) development of failure process along the interfaces located on the two crack lines of the direct shear test, and to the different stress states existing in the interfaces on the top and bottom extremes of both crack lines with respect to the others along these lines. The failure initiates in the interfaces located on the extremes of the lines where the interfaces are placed. Due to the cohesive type of

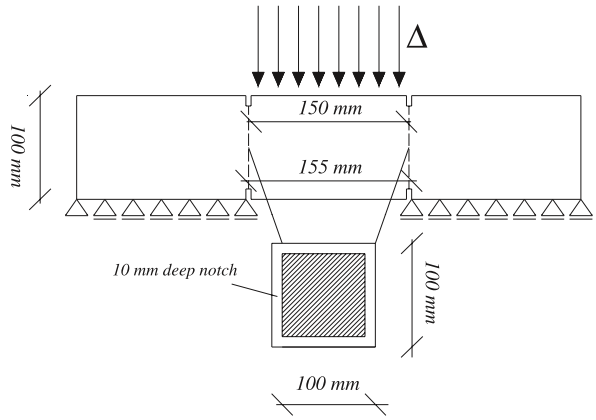

Fig. 17. Specimen geometry and boundary condition of the direct shear test according to Boulekbache et al. [44].

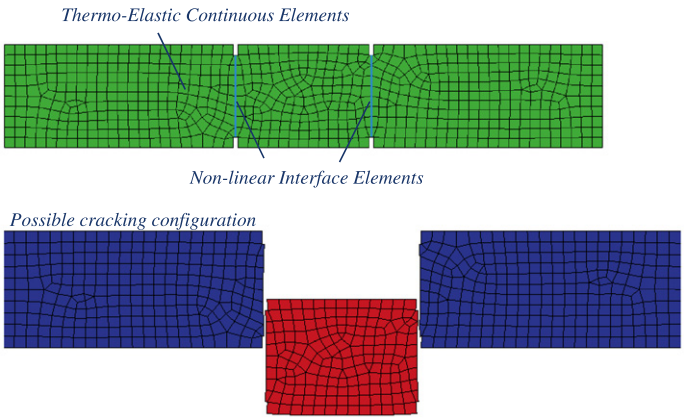

Fig. 18. Finite element mesh, interfaces and possible cracked configuration of the direct shear test.

failure criterion, the tangential displacements activated during failure processes of the interfaces on the bottom and top extremes, give rise to normal displacements in the same interfaces. Consequently, and due to the pure elastic behavior of the continuum elements, the second line of interfaces are subjected to higher confinement and, therefore, their failure criteria are reached at higher shear stresses. As it can be observed in the same Fig. 19, this effect is mitigated by increasing temperature as in this case the post-peak strength decay of the interfaces is less pronounced, leading to an increasing redistribution of the failure or damage zone among other interfaces in the neighborhood. The discontinuity in the ascending branch of concrete elements under low temperature ($T < 400\,^{\circ}\mathrm{C}$) can be mitigated by sufficient mesh refinement, i.e., by shortening the interfaces. However, this is not analyzed in this section as the main objective of the results in Fig. 19 is to show the strong influence of the proposed temperature dependent non-linear interface model on the overall response behavior of structural components when subjected to different thermo–mechanical conditions. As a matter of fact, these results demonstrate the capabilities of the proposed interface formulation to reproduce failure processes of concrete beams when subjected to severe thermal damage.

Fig. 20 highlights the variation with the temperature of the energy released under mode II type of fracture ($G_{f\,II}$ as predicted by the model) along all interfaces located in the two active shear cracks in the direct shear test of Fig. 18. These results clearly demonstrate that the energy released under mode II type of fracture represents the controlling parameter of the post-peak ductility degradation due to temperature that takes place in these tests.

Unfortunately experimental studies are currently not available in literature related to failure analysis of concrete components subjected to shear and high temperature. This is a considerable limitation for the verification of model

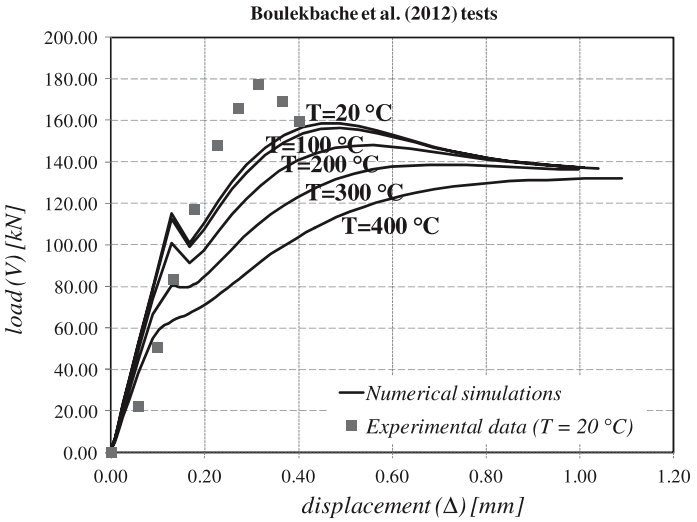

Fig. 19. Shear load–displacement response: experimental results by Boulekbache et al. [44] and numerical predictions.

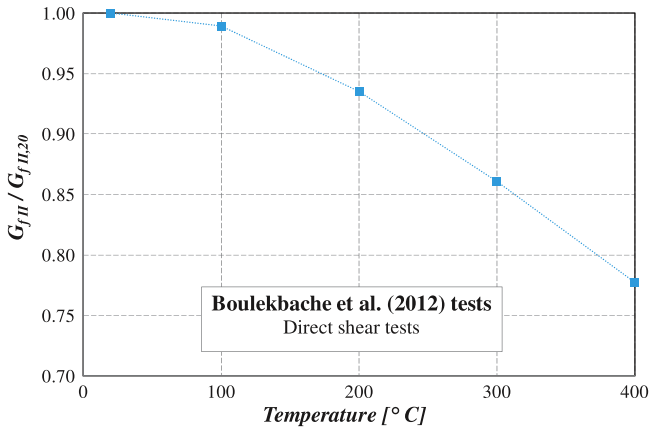

Fig. 20. Ratio between the energy released under mode II type of fracture ($G_{f\,II}$) and that of reference at 20 °C ($G_{f\,II,20}$) vs. Temperature: numerical results of direct shear test by Boulekbache et al. [44].

predictions. Nevertheless, as demonstrated here, the proposed non-linear interface model is able to provide expected results and to reproduce the influence of temperature effects on the overall mechanical response.

7. Concluding remarks

This paper addressed the formulation of a novel coupled thermo–mechanical model for concrete interfaces subjected to high temperatures combined with mechanical loads. This proposal took into account a quadratic hyperbola as a maximum strength criterion for the interface, defining the interaction between maximum shear and normal interface stresses. Such a formulation explicitly considered the thermal effects into the failure criterion and the resulting post-cracking response through a new temperature-based scaling function affecting the strength parameters and the softening law. Numerical analyses, performed with the constitutive model presented in this paper, demonstrated its predictive capabilities in terms of the most relevant aspects of the mechanical behavior of concrete under high temperatures.

The proposed interface model can also be employed in mesoscopic analyses using mortar–mortar and mortar-aggregate interfaces aimed at simulating failure processes of concrete specimens under high temperatures. However, this aspect is beyond the scopes of the present paper and will be addressed in future developments of the current research.

Acknowledgments

The authors acknowledge the financial support for this work provided by CONICET (Argentine National Council for Science and Technology) through the Grant No. PIP 112-200801-00707, CIUNT (Research Council University of Tucuman) through the Grant No. E/26 479 and University of Buenos Aires through the Grant No. 20020090100 139.

Moreover, the support to networking activities provided by "Encore" Project (FP7-PEOPLE-2011-IRSES n 295283; http://www.encore-fp7.unisa.it/) funded by the European Union within the Seventh Framework Programme is also gratefully acknowledged.

Appendix

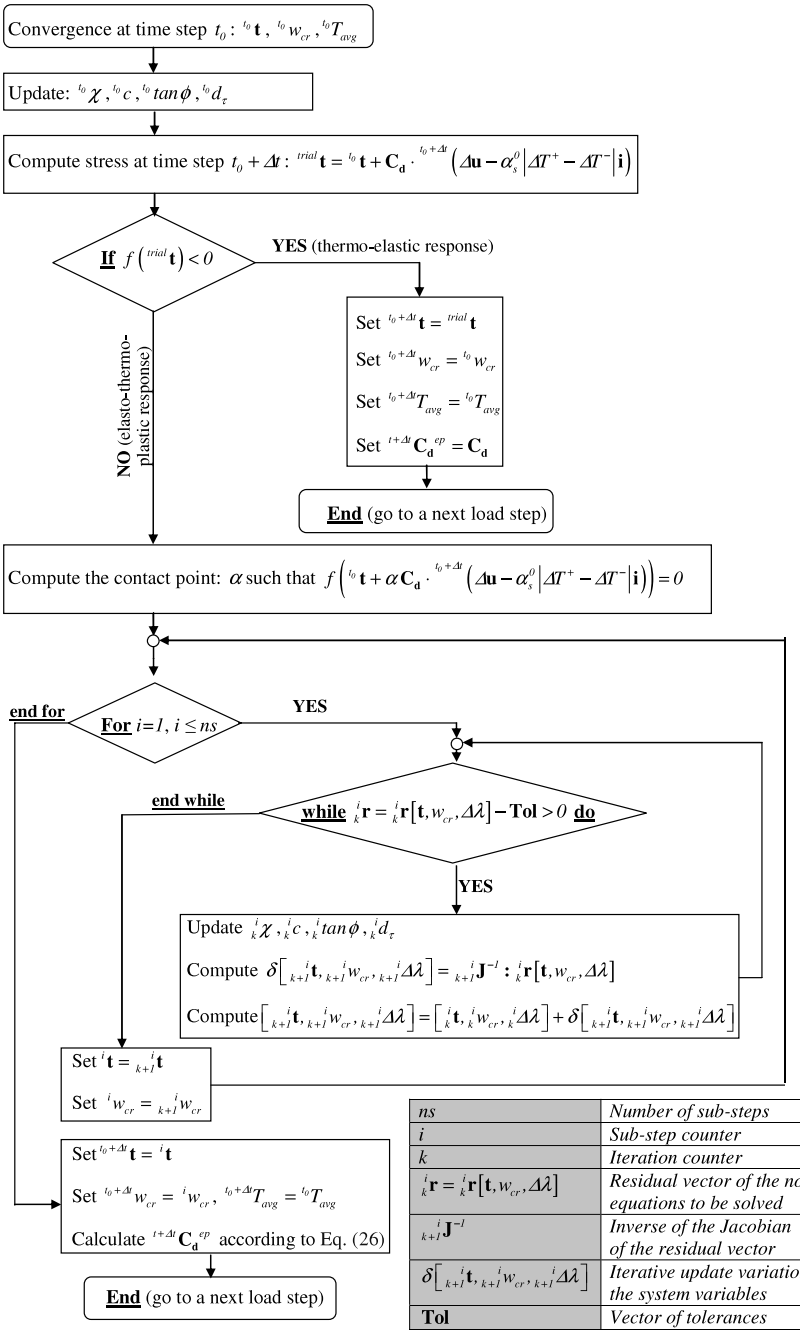

ns	*Number of sub-steps*
i	*Sub-step counter*
k	*Iteration counter*
${}^i_k\mathbf{r} = {}^i_k\mathbf{r}\left[\mathbf{t}, w_{cr}, \Delta\lambda\right]$	*Residual vector of the non-linear equations to be solved*
${}^i_{k+1}\mathbf{J}^{-1}$	*Inverse of the Jacobian of the residual vector*
$\delta\left[{}^i_{k+1}\mathbf{t}, {}^i_{k+1}w_{cr}, {}^i_{k+1}\Delta\lambda\right]$	*Iterative update variations of the system variables*
Tol	*Vector of tolerances*

Flowchart of local Newton's method aimed at describing the step-by-step integration of the elasto–thermo–plastic interface model.

References

[1] M. Ripani, G. Etse, S. Vrech, J. Mroginski, Thermodynamic gradient-based poroplastic theory for concrete under high temperatures, Int. J. Plast. 61 (2014) 157–177.
[2] D. Gawin, F. Pesavento, B. Schrefler, Modelling of hygro-thermal behaviour of concrete at high temperature with thermo-chemical and mechanical material degradation, Comput. Methods Appl. Mech. Engrg. 192 (2003) 1731–1771.
[3] O. Bahr, P. Schaumann, B. Bollen, J. Bracke, Young's modulus and Poisson's ratio of concrete at high temperatures: experimental investigations, Mater. & Des. 45 (2013) 421–429.
[4] J. Piasta, Heat deformations of cement paste phases and the microstructure of cement paste, Mater. Constr. 17 (1984) 415–420.
[5] A.B. Kizilkanat, N. Yuzer, N. Kabay, Thermo-physical properties of concrete exposed to high temperature, Constr. Build. Mater. 45 (2013) 157–161.
[6] H. Tanyildizi, A. Coskun, The effect of high temperature on compressive strength and splitting tensile strength of structural lightweight concrete containing fly ash, Constr. Build. Mater. 22 (2008) 2269–2275.
[7] Z. Guo, X. Shi, Strength of concrete at elevated temperatures, in: Experiment and Calculation of Reinforced Concrete at Elevated Temperatures, Butterworth-Heinemann, 2011, pp. 2–16. (Chapter 1).
[8] L.T. Phan, N.J. Carino, Effects of test conditions and mixture proportions on behavior of high-strength concrete exposed to high temperatures, ACI Mater. J. 99 (2002) 54–66.
[9] ACI-216.1-07, Code Requirements for Determining Fire Resistance of Concrete and Masonry Construction Assemblies, Fire Resistance and Fire Protection of Structures–Joint ACI-TMS, ACI Committee, USA, 2007.
[10] EN-1992-1.2, EN, Part 1.2 design of concrete structures. Structural fire design, Eurocodes, 2010.
[11] W. Nechnech, F. Meftah, J. Reynouard, An elasto–plastic damage model for plain concrete subjected to high temperatures, Eng. Struct. 24 (2002) 597–611.
[12] B.A. Schrefler, C.E. Majorana, G.A. Khoury, D. Gawin, Thermo-hydro-mechanical modelling of high performance concrete at high temperatures, Eng. Comput. 19 (2002) 787–819.
[13] S.D. Pont, S. Durand, B. Schrefler, A multiphase thermo-hydro-mechanical model for concrete at high temperatures—finite element implementation and validation under loca load, Nucl. Eng. Des. 237 (2007) 2137–2150.
[14] R. Tenchev, P. Purnell, An application of a damage constitutive model to concrete at high temperature and prediction of spalling, Internat. J. Solids Structures 42 (2005) 6550–6565.
[15] X. Lei, Contact friction analysis with a simple interface element, Comput. Methods Appl. Mech. Engrg. 190 (2001) 1955–1965.
[16] P. Wriggers, G. Zavarise, Computational Contact Mechanics, Wiley Online Library, 2002.
[17] A. Kinloch, E. Busso, F. Matthews, Y. Qiu, J. Chen, M. Crisfield, Predicting progressive delamination of composite material specimens via interface elements, Mech. Compos. Mater. Struct. 6 (1999) 301–317.
[18] H.A. Baky, U. Ebead, K. Neale, Nonlinear micromechanics-based bond–slip model for FRP/concrete interfaces, Eng. Struct. 39 (2012) 11–23.
[19] A. Caggiano, E. Martinelli, A unified formulation for simulating the bond behaviour of fibres in cementitious materials, Mater. Des. 42 (2012) 204–213.
[20] D. Xie, S.B. Biggers Jr., Progressive crack growth analysis using interface element based on the virtual crack closure technique, Finite Elem. Anal. Des. 42 (2006) 977–984.
[21] D. Ciancio, I. Carol, M. Cuomo, A method for the calculation of inter-element stresses in 3D, Comput. Methods Appl. Mech. Engrg. 254 (2013) 222–237.
[22] S.C. D'Aguiar, A. Modaressi-Farahmand-Razavi, J.A. dos Santos, F. Lopez-Caballero, Elastoplastic constitutive modelling of soil–structure interfaces under monotonic and cyclic loading, Comput. Geotech. 38 (2011) 430–447.
[23] T. Stankowski, K. Runesson, S. Sture, Fracture and slip of interfaces in cementitious composites. I: characteristics, II: implementation, ASCE-J. Eng. Mech. 119 (1993) 292–327.
[24] C.M. Lopez, I. Carol, A. Aguado, Meso-structural study of concrete fracture using interface elements. I: numerical model and tensile behavior, Mater. Struct. 41 (2008) 583–599.
[25] C.M. Lopez, I. Carol, A. Aguado, Meso-structural study of concrete fracture using interface elements. II: compression, biaxial and brazilian test, Mater. Struct. 41 (2008) 601–620.
[26] R. Lorefice, G. Etse, I. Carol, Viscoplastic approach for rate-dependent failure analysis of concrete joints and interfaces, Internat. J. Solids Structures 45 (2008) 2686–2705.
[27] A. Caggiano, G. Etse, E. Martinelli, Zero-thickness interface model formulation for failure behavior of fiber-reinforced cementitious composites, Comput. Struct. 98–99 (2012) 23–32.
[28] G. Etse, A. Caggiano, S. Vrech, Multiscale failure analysis of fiber reinforced concrete based on a discrete crack model, Int. J. Fract. 178 (2012) 131–146.
[29] A. Caggiano, G. Etse, E. Martinelli, Interface model for fracture behaviour of fiber-reinforced cementitious composites (FRCCs): Theoretical formulation and applications, J. Environ. Civ. Eng., 15 (9), 1339–1358.
[30] J. Segura, I. Carol, On zero-thickness interface elements for diffusion problems, Int. J. Numer. Anal. Methods Geomech. 28 (2004) 947–962.
[31] A.E. Idiart, C.M. López, I. Carol, Modeling of drying shrinkage of concrete specimens at the meso-level, Mater. Struct. 44 (2011) 415–435.
[32] A.E. Idiart, C.M. Lopez, I. Carol, Chemo-mechanical analysis of concrete cracking and degradation due to external sulfate attack: a meso-scale model, Cem. Concr. Compos. 33 (2011) 411–423.

[33] J. Liaudat, M. Rodriguez, C. Lopez, I. Carol, Mechanics and Physics of Creep, Shrinkage, and Durability of Concrete: A Tribute to Zdenek P. Bažant: Proceedings of the Ninth International Conference on Creep, Shrinkage, and Durability Mechanics (CONCREEP-9), September 22–25, 2013, ASCE Publications, Cambridge, Massachusetts, 2013.
[34] I. Carol, P. Prat, C. Lopez, Normal/shear cracking model: applications to discrete crack analysis, ASCE-J. Eng. Mech. 123 (1997) 765–773.
[35] Z. Bažant, L. Najjar, Nonlinear water diffusion in nonsaturated concrete, Matér. Constr. 5 (1972) 3–20.
[36] K. van Breugel, E. Koenders, Numerical simulation of hydration-driven moisture transport in bulk and interface paste in hardening concrete, Cem. Concr. Res. 30 (2000) 1911–1914.
[37] E. Koenders, K. Van Breugel, Numerical modelling of autogenous shrinkage of hardening cement paste, Cem. Concr. Res. 27 (1997) 1489–1499.
[38] E. Martinelli, E.A. Koenders, A. Caggiano, A numerical recipe for modelling hydration and heat flow in hardening concrete, Cem. Concr. Compos. 40 (2013) 48–58.
[39] K. Willam, I. Rhee, B. Shing, Interface damage model for thermomechanical degradation of heterogeneous materials, Comput. Methods Appl. Mech. Engrg. 193 (2004) 3327–3350.
[40] A. Caballero, K. Willam, I. Carol, Consistent tangent formulation for 3D interface modeling of cracking/fracture in quasi-brittle materials, Comput. Methods Appl. Mech. Engrg. 197 (2008) 2804–2822.
[41] P. Bamonte, R. Felicetti, On the tensile behavior of thermally-damaged concrete, in: Proceedings of the 6th International Conference on Fracture Mechanics of Concrete and Concrete Structures, Taylor & Francis, London, UK, 2007, pp. 1715–1722.
[42] M. Hassanzadeh, Determination of fracture zone properties in mixed mode I and II, Eng. Fract. Mech. 35 (1990) 845–853.
[43] B. Barragan, A. Di Maio, G. Giaccio, L. Traversa, R. Zerbino, Efecto de las altas temeperaturas sobre las propiedades fisicomecanicas del hormigon, Cienc. Tecn. Hormig. LEMIT 5 (1997) 51–64.
[44] B. Boulekbache, M. Hamrat, M. Chemrouk, S. Amziane, Influence of yield stress and compressive strength on direct shear behaviour of steel fibre-reinforced concrete, Constr. Build. Mater. 27 (2012) 6–14.